

XAFS spectroscopy; fundamental principles and data analysis

D.C. Koningsberger^{a,*}, B.L. Mojet^{a,**}, G.E. van Dorssen^a and D.E. Ramaker^b

^a Department of Inorganic Chemistry and Catalysis, Debye Institute, Utrecht University, PO Box 80083, 3508 TB Utrecht, The Netherlands

^b Department of Chemistry and Materials Science Institute, George Washington University, Washington, DC 20052, USA

The physical principles of XAFS spectroscopy are given at a sufficiently basic level to enable scientists working in the field of catalysis to critically evaluate articles dealing with XAFS studies on catalytic materials. The described data-analysis methods provide the basic tools for studying the electronic and structural properties of supported metal, metal–oxide or metal–sulfide catalysts. These methods include (a) fitting in R -space, (b) application of the difference file technique and (c) control of the fit procedure with k^1 and k^3 weighting with the help of phase- and amplitude-corrected Fourier transforms.

Keywords: XAFS physical principles, XAFS data analysis, fitting in R -space, detection of low Z scatterers, phase- and amplitude-corrected Fourier transforms, difference file technique, use of theoretical references

1. Introduction

XAFS spectroscopy is the only spectroscopic technique that provides information on the electronic and structural properties of catalysts under reaction conditions and in the presence of reactants. This is true, because XAFS is one of only a few probes that utilises photons exclusively (i.e., photons in and using transmission or fluorescence yield photons out). X-ray diffraction (XRD) is similar in this regard, but it requires long-range order and provides only geometric information. X-ray photoelectron spectroscopy (XPS), as well as any other electron spectroscopy such as Auger, provides electronic information but requires ultra-high vacuum conditions. XAFS has been limited until recently to providing geometric information on systems with short-range order. However, recent advances to be discussed in this volume, have extended XAFS to also provide electronic structure. Thus XAFS is ideal for the study of catalysts, both under realistic reaction conditions, as well as in vacuum.

This paper describes the physical principles of XAFS spectroscopy at a sufficiently basic level to allow scientists working in the field of catalysis to critically evaluate recent articles in the literature dealing with the application of the XAFS technique in catalysis research. The data-analysis methods given here form the basic tools to unravel the electronic and structural properties of homogeneous and heterogeneous catalysts, which consist of metal particles, metal sulfides or metal oxides dispersed onto different supports. The basic tools include: (a) fitting in R -space, (b) application of the difference file technique and (c) control of the fit procedure with k^1 and k^3 weighting with the help of phase- and amplitude-corrected Fourier transforms. These basic tools provide the possibility to study not only the structure of the supported catalysts, but also the interaction

between the catalysts and the support. The use of calibrated theoretical references makes it possible to analyse EXAFS data down to very low values of k . This allows for a more accurate determination of the low Z scatterers present in the EXAFS data. Moreover, it is then also possible to isolate the atomic XAFS contribution from the first-shell EXAFS contributions.

2. Physical principles

2.1. Absorption and scattering of X-rays

When a beam of X-ray photons passes through a material, the incident intensity I will be decreased by an amount that is determined by the absorption characteristics of the material being irradiated. For a path length dx of the radiation through the material the decrease dI is given by

$$dI = -\mu(E)I dx \quad (1)$$

with the linear absorption coefficient $\mu(E)$ a function of the photon energy. Integrating equation (1) over the total thickness x yields Lambert's law,

$$I_t = I_0 e^{-\mu(E)x}. \quad (2)$$

The X-ray absorption spectrum exhibits a generally smooth decreasing intensity to higher energy. When the energy of the incoming photons is large enough to excite an electron from a deeper core level to a vacant excited state or to the continuum (e.g., after the absorption edge), a sharp rise in the absorption intensity appears. This sharp rise is denoted as the threshold energy or absorption edge. At the absorption edge, E_{edge} , the kinetic energy of the electron (E_k) is defined to be equal to E_0 , often referred to as the zero-point energy or "inner potential". For any energy above this, the photoelectron kinetic energy is given by

$$E_k = h\nu - E_{\text{binding}}. \quad (3)$$

* To whom correspondence should be addressed.

** Present address: Schuit Institute of Catalysis, Eindhoven University of Technology, PO Box 513, 5600 MB Eindhoven, The Netherlands.

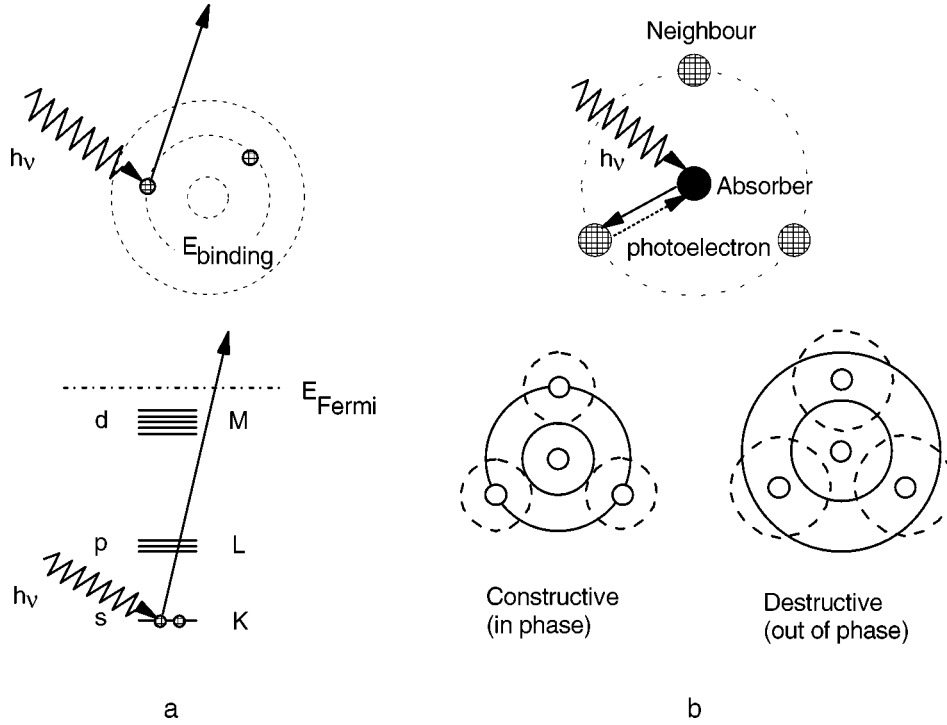


Figure 1. (a) Schematic illustration of the photoelectric effect in terms of excitation of the different orbital (top) or different energy levels (bottom), (b) illustration of neighbouring shells of atoms about the absorber (top) and constructive (in phase) or destructive (out of phase) interference between outgoing photoelectron wave and backscattered off this shell of neighbouring atoms (bottom).

Quantum mechanically the outgoing photoelectron can be represented as a spherical wave with wavelength λ defined as

$$\lambda = 2\pi/k,$$

and

$$k = \sqrt{\left(\frac{8\pi^2m}{h^2}\right)(h\nu + E_0 - E_{\text{edge}})}, \quad (4)$$

with k the wave-vector, m the electron mass and h Planck's constant.

The linear absorption coefficient $\mu(E)$ is proportional to the transition probability of the photoelectric event. According to Fermi's Golden Rule the transition probability is (within the dipole approximation) a function of the initial-state and final-state wave functions [1]:

$$\mu(E) = C |\langle \psi_f | \hat{e}r | \psi_i \rangle|^2 \delta(E_f - E_i - h\nu). \quad (5)$$

Here \hat{e} is the electric field polarisation vector of the photon, and r the coordinate vector of the electron. The dipole approximation is only valid when the wavelength of the photons is larger than the size of the absorbing atom. The final state wave function ψ_f consists of two main parts, namely the outgoing electron wave and a backscattered electron wave

$$\psi_f = \psi_{\text{outgoing}} + \psi_{\text{backscattered}}. \quad (6)$$

Interference between these two final-state wave functions causes the observed fine structure in X-ray absorption spectra. Figure 1(a) shows a schematic representation of the

photoelectric effect, that is, the interaction of an X-ray photon with matter producing a photoelectron with a kinetic energy given by (3). Figure 1(b) makes clear that the outgoing electron can be viewed as a spherical wave that scatters off neighbouring atoms (e.g., electron density), producing a backscattered wave. The outgoing and backscattered waves interfere, causing an interference pattern varying between total construction (the two waves are fully in phase) or total destruction (the two waves are exactly out of phase). Since the path lengths of both waves define their final phase, it can be seen that the distance to the neighbouring atoms determines the interference pattern. Equation (5) shows that the absorption coefficient is proportional to the transition probability defined by the matrix element.

The absorption coefficient exhibits a fine structure because the final wave state function is modulated due to the interference pattern. As a result, the absorption coefficient above the absorption edge is defined as

$$\mu_{\text{total}} = \mu_0 [1 + \chi_{\text{EX}}], \quad (7)$$

with μ_0 representing the atomic background. χ_{EX} forms the oscillatory part of the total absorption, describing the scattering of the outgoing electron against the neighbouring atoms. It is called the EXAFS function. Since the oscillatory part is created by the interference between the outgoing and backscattered waves, χ_{EX} contains information about the local structure around the absorber atom. The fact that a specific photon energy is needed to excite electrons, makes X-ray absorption spectroscopy an element specific technique. It will be shown in a subsequent pa-

per [2] that in fact μ_0 can be written as $\mu_0 = \mu_{\text{free}}(1 + \chi_{\text{AX}})$ with μ_{free} the free atomic background and χ_{AX} the atomic XAFS function representing the scattering of the outgoing electron against the periphery of the X-ray absorber atom itself.

2.2. The EXAFS equation

Several authors have given derivations for the EXAFS theory [3–6]. The simplest theory is based on the single-scattering plane-wave approximation. In this approximation the electron wave is viewed as a plane wave, rather than a spherical wave to simplify the mathematical derivation. The plane-wave approximation assumes that the atomic radii are much smaller than the inter-atomic distances, and is valid only for higher k -values ($k > 3 \text{ \AA}^{-1}$) (see equation (4)). At lower k -values the curved wave, or spherical wave, theory has to be used, to give reasonable agreement with experiment.

Here only the equations obtained from the plane-wave approximation will be given. In the single-scattering event, the electron is assumed to be scattered only once before it returns to the absorber atom. This simplification is sufficient to describe and analyse the EXAFS signals in most experimental data. The χ function can be given as a summation over all interference patterns (sine waves) scattered off of all neighbouring atoms:

$$\chi(k) = \sum_{j=1}^{\text{Shells}} A_j(k) \sin \Phi_j(k). \quad (8)$$

A coordination shell is defined by the identity of the scattering atom and the distance from the absorber atom. The fact that $\chi(k)$ is a summation over all coordination shells around a specific absorbing element, emphasises that X-ray absorption is a bulk technique, sampling all atoms of a particular absorber element equally; this element is determined by the photon energy region examined. The EXAFS function will give information about the average coordination around the absorbing element.

Equation (8) shows that the EXAFS formula consists of two main parts, the amplitude $A_j(k)$ and a sine function describing the interference pattern. The argument of the sine function $\Phi_j(k)$ consists of the inter-atomic distance between the absorber and scatterer atoms and a phase factor,

$$\sin \Phi(k) = \sin [2kR_j - \phi_j(k)]$$

with

$$\phi_j(k) = 2\phi_{\text{absorber}}(k) + \phi_{\text{scatterer}}(k). \quad (9)$$

The ‘‘sin’’ function accounts for the oscillations seen in the EXAFS. The argument inside the sin function can be thought of as being related to the time for the electron to travel to the neighboring atom and return. In figure 2, $2kR$ would represent this time if the kinetic electron were constant across the entire R -range. However, it is altered by an amount, $\phi_{\text{scatterer}}$, resulting in part from the increase in

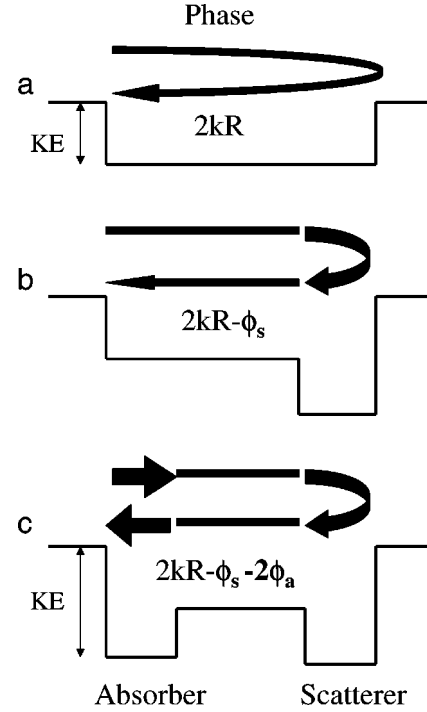


Figure 2. Schematic illustration of the contributions to the total phase in the EXAFS sine function. The thickness of the arrows is suggestive of the relative speeds of the photoelectron. (a) The phase delay is equal to $2kR$, reflecting the time required for the photoelectron to travel out to the scatterer atom and return, (b) this phase is decreased by an amount ϕ_s because near the scatterer the kinetic energy of the electron is increased thereby decreasing the time required to transverse the $2R$ distance (represented by thick arrow at the scatterer) and (c) the phase is decreased by the additional term $2\phi_a$ because near the absorber core the photoelectron kinetic energy is also larger (represented by thick arrows at the absorber).

velocity of the photoelectron as it approaches the neighbouring atom and then slows again as it returns. A similar phase shift, $2\phi_{\text{absorber}}$, results from the absorber atom itself. The velocity increases as it approaches an atom because as shown in figure 2, the potential that an electron experiences decreases to more negative values as the electron is attracted more by the nucleus, and hence its kinetic energy increases. For convenience, this atomic potential is ‘‘squared off’’ in figure 2.

The amplitude $A_j(k)$ contains the coordination number (N) and disorder (σ), which is the fluctuation in R_j due to thermal motion or structural disorder:

$$A_j(k) = \frac{N_j}{kR_j^2} S_0^2 F_j(k) e^{-2k^2\sigma_j^2} e^{-2R_j/\lambda k}, \quad (10)$$

where $F_j(k)$ is the backscattering amplitude, which is element specific. S_0^2 is an amplitude reduction factor representing many-body effects such as central atom shake-up and shake-off due to relaxation processes after the photoionisation event [6,7]. The exponential term containing the mean-free path, λ , of the photoelectrons accounts for the finite lifetime of the excited state.

The outgoing electron wave is scattered primarily off the bound electrons of the neighbouring atoms. Backscattering

is resonant in nature; thus the backscattering amplitude is enhanced at those energy values of the photoelectron that are equal to the orbital energies in the backscattering atom (see also figure 3). As each atom has its unique electron configuration, it will have a unique backscattering pattern as a function of k [6,7]. Figure 4 shows the backscattering amplitudes $F'(k)$ as a function of k as calculated with the FEFF7.02 code for Pt–Pt, Pt–O and Pt–H absorber–scattering pairs. To reveal the resonant nature of scattering, the binding energies of some bound electrons in the scattering atoms are also shown in figure 4. The binding energy E_b is converted to k according to the equation noted in the caption of figure 4. It can clearly be seen that the backscattering intensity enhances at those energy values of the photoelectron that are equal to the orbital energies of the respective atoms. Thus, for hydrogen as scatterer only one maximum is observed in the backscattering amplitude at low k ($\sim 2 \text{ \AA}^{-1}$), after which the scattering dies out

fast. For oxygen as scatterer two maxima are visible, one caused by scattering off the 2p orbital electrons, and the second by scattering off the 2s. Around $k = 11 \text{ \AA}^{-1}$ a small shoulder is visible due to scattering off the 1s electrons of oxygen. The backscattering amplitude for Pt shows four maxima caused by, respectively, 5d, 5p-4f-5s, 4d and 4p-4s electrons. This figure clearly shows the resonant nature of the scattering, i.e., the outgoing photoelectron and the bound electrons off which the photoelectron is scattered tend to have equal kinetic energies. The data for Pt–Pt also reveal the dramatic increase in the backscattering cross-section with increasing k -values (or energy).

The above equations are given for a L_{II} or L_{III} transition, in which only the p to d electron transition is taken into account, as the p to s transition is much weaker [8]. For K-edges the same formula with an overall minus sign can be used. In the derivation of the EXAFS equation multiple scattering paths are neglected as they only contribute a few percent to the total scattering off neighbouring atoms. However, just after the absorption edge, where the photoelectron has a long mean-free path multiple scattering becomes very significant (XANES region).

Scattering

Kinetic energy of photo-electron =
Kinetic energy of bound electron

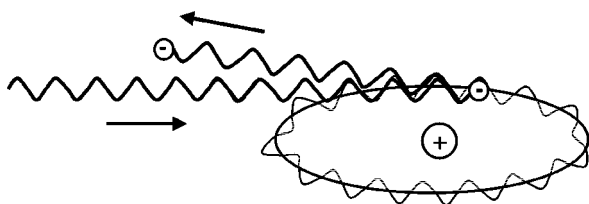


Figure 3. Schematic illustration of resonant scattering where the kinetic energy of the photoelectron is equal to the orbital kinetic energy of the electron causing the scattering. This is indicated by the roughly equal wavelength in the waves.

3. Data analysis

3.1. Isolating $\chi(k)$ from experimental data

The extraction of $\chi(k)$ from the experimentally obtained μ_{total} follows several consecutive steps, that are visualised in figure 5. As defined in equation (7), χ can be obtained once the atomic absorption is known, by calculating

$$\chi = \frac{\mu_{\text{total}} - \mu_{\text{atomic}}}{\mu_{\text{atomic}}} \quad (11)$$

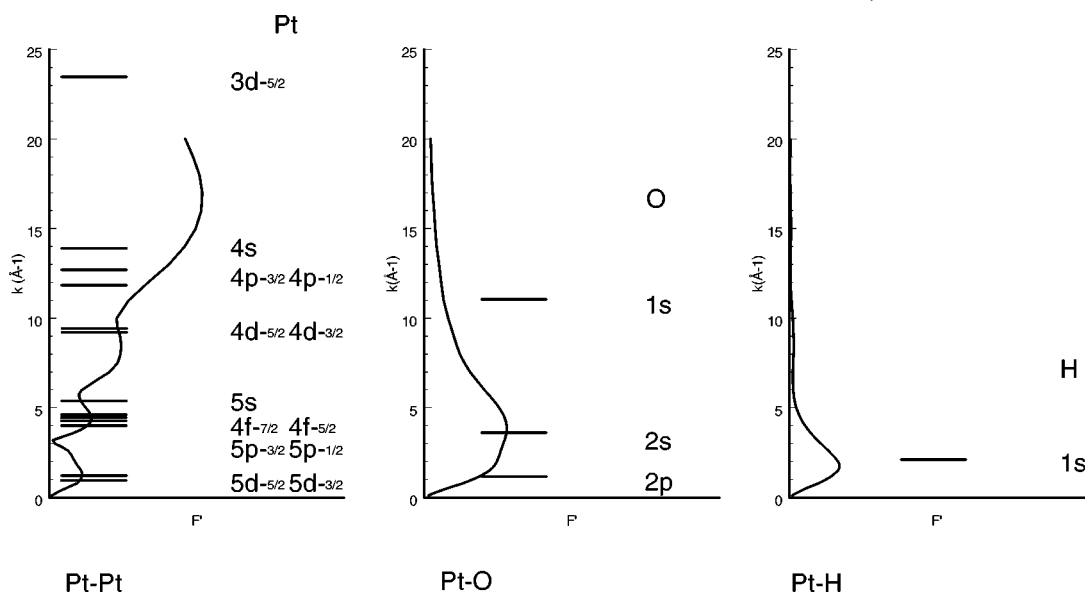


Figure 4. Backscattering amplitude $F'(k)$ as a function of k for Pt–Pt, Pt–O and Pt–H EXAFS. E_{binding} is converted to k -space according to $k = \sqrt{(2m/\hbar^2)E_{\text{binding}}}$.

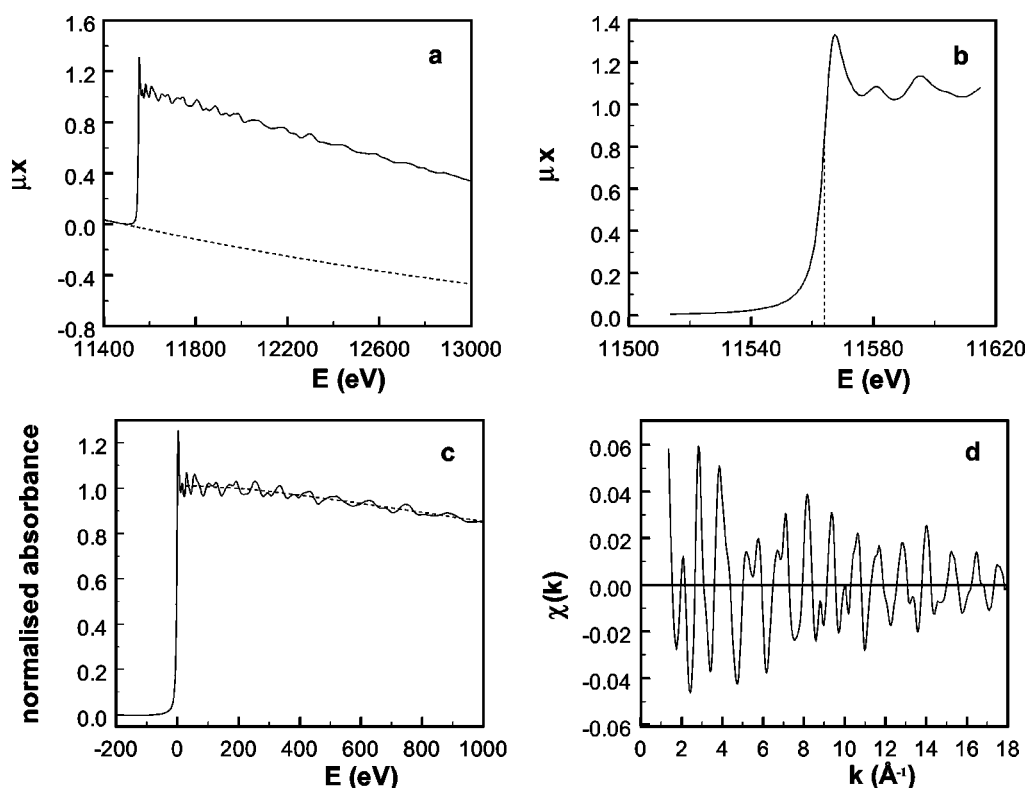


Figure 5. The different steps for extraction of the oscillatory part of an X-ray absorption spectrum, shown here at the L_3 edge for platinum foil: (a) pre-edge background removal (---); (b) edge position determination, typically chosen at the inflection point; (c) post-edge background removal (---) and normalisation; (d) transforming of the EXAFS spectrum to k scale through equation (4) after normalisation (not shown).

Before μ_{atomic} can be determined, the pre-edge (X-ray absorption before the actual absorption edge occurs) has to be subtracted (figure 5(a)). The pre-edge is normally approximated by a modified Victoreen [6] and calculated by extrapolation of the pre-edge region in the data.

After the pre-edge subtraction the edge energy (e.g., E_{edge}) has to be defined (figure 5(b)). The value of the edge energy is used to calculate k (\AA^{-1}) as given in (4). The choice for this energy is rather arbitrary. The inflection point (i.e., the maximum in the first derivative of the absorption edge) is generally considered as a systematic choice. However, the presence of resonances or electronic excitations can cover up the exact position of E_{edge} . To avoid this complexity, the position of the half height (0.5–0.6) of the normalised edge is often chosen as E_{edge} . The inner potential, E_0 , is often chosen to be zero.

The atomic background (μ_{atomic}) after the absorption edge has to be determined (figure 5(c)), normally using a cubic spline [9]:

$$\sum_{i=1}^{\text{NPTS}} \frac{(\mu x_i - BCK_i)^2}{e^{-WEk_i^2}} \leq \text{SM}. \quad (12)$$

The cubic spline consists of four parameters that define the spline function: SM (smoothing parameter), W (weighting factor) and the start and end energy that determine the number of points. The more data points available, the better the spline will be defined. The background is optimised using several criteria, of which the most important is not to

remove any of the oscillating information from your data. Since it has been shown recently [2,10,11] that important information can be obtained from the atomic XAFS contribution, both χ_{EX} and χ_{AX} have to be separated from the free atomic background. This can be accomplished by a procedure, described in detail in the following paper of this volume [2].

Before $\chi(k)$ can be obtained, the total absorption as obtained from experiment has to be normalised per absorber atom. Generally, spectra are normalised by division of the absorption data by the edge-step at 50 eV after the absorption edge (figure 5(c)). Finally, $\chi(k)$ is calculated according to (11) (figure 5(d)).

3.2. Fourier transformation

Sayers et al. [5] have shown in 1971 that Fourier transformation of $\chi(k)$ results in a radial distribution function (figure 6). The Fourier transformation is defined by

$$\text{FT}(R) = \frac{1}{\sqrt{2\pi}} \int_{k_{\text{min}}}^{k_{\text{max}}} k^n \chi(k) e^{i2kR} dk. \quad (13)$$

The radial distribution function is defined in R -space (e.g., distance from the absorber atom). The distance found in the Fourier transformation is about 0.2–0.5 \AA shorter than the actual distance due to the energy dependence of the phase factors in the sine function (see equation (9)). The Fourier transform can be taken with different k weightings

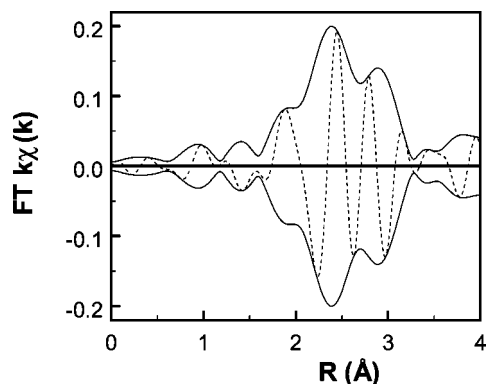


Figure 6. Radial distribution function ($0 < R < 4 \text{ \AA}$) after Fourier transformation (k^1 , $\Delta k = 2.6\text{--}18.6 \text{ \AA}^{-1}$) of $\chi(k)$ of Pt foil. Absolute part (—) and imaginary part (- -).

(multiplication by k^n). This can be used to distinguish between high and low Z scatterers around the absorber atom. An element with low mass (like oxygen) will scatter mainly at lower k -values, while platinum (high mass) will scatter significantly at higher k -values as shown in figure 4. Weighting of the Fourier transformation will, therefore, emphasise the important scatterer in a specific region.

Since the Fourier transform is a complex function, both real and imaginary parts are obtained. The envelope (absolute part) of the Fourier transform is defined by

$$\text{absolute part} = \sqrt{\text{Im}^2 + \text{Re}^2}. \quad (14)$$

Figure 6 shows both the absolute and imaginary part of the Fourier transform for Pt foil. The absolute part is determined mainly by the number of neighbours and disorder. The imaginary part is very useful in the analysis of EXAFS data for an accurate determination of the absorber–scatterer distance and for the discovery of unknown contributions when analysing EXAFS data.

3.3. Fourier filtering

In addition to forward Fourier transformation, coordination shells can be isolated (filtered) using the inverse Fourier transformation, which results in a $\chi_j(k)$ function for that specific shell. This method can be very useful in analysing data or obtaining standards for phase shifts and backscattering amplitudes from reference compounds that are needed in EXAFS data analysis. Figure 7(a) demonstrates the Fourier filtering of the first Pt–Pt shell of Pt foil. The forward Fourier transform is taken with a k^3 weighting from $k = 1.9$ to 18.6 \AA^{-1} . The first-shell Pt–Pt peak is Fourier filtered from $R = 1.6$ to 3.2 \AA . The isolated first-shell Pt–Pt EXAFS is plotted in figure 7(b) with a dotted line superimposed onto the original EXAFS function (solid line). Some Fourier filtering errors occur over a region of about $\Delta k = 1 \text{ \AA}^{-1}$ at the start and the end of the isolated first-shell Pt–Pt EXAFS [12]. This region should be avoided in analysing Fourier filtered data. The Fourier transforms (k^3 , $\Delta k = 2.6\text{--}17.8 \text{ \AA}^{-1}$) of the raw EXAFS data and the isolated first-shell data are shown in figure 7(c) with a solid

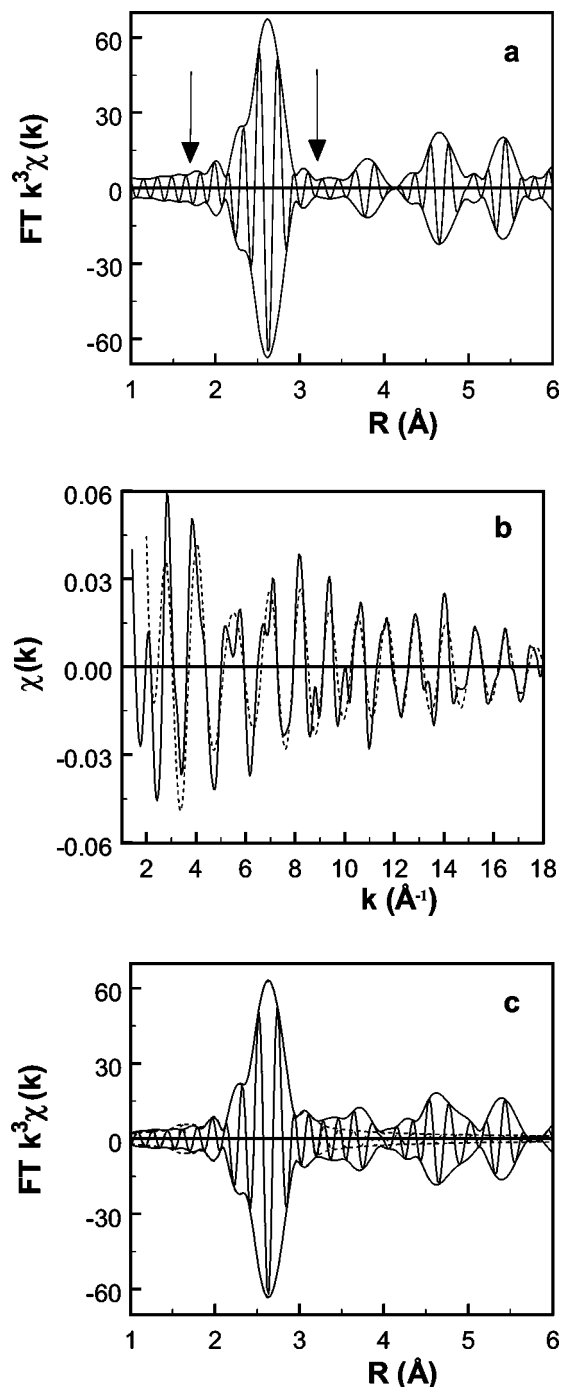


Figure 7. Isolation of one coordination shell and back-transformation to k -space (i.e., Fourier filtering). (a) Fourier transform (k^3 , $\Delta k = 1.9\text{--}18.6 \text{ \AA}^{-1}$) of data; arrows indicate R -space window used for filtering. (b) Experimental EXAFS data (—) and isolated first-shell Pt–Pt (- - -) by Fourier filtering using window as defined with arrows in (a). (c) Forward transform (k^3 , $\Delta k = 2.6\text{--}17.8 \text{ \AA}^{-1}$) of experimental data (—) and Fourier filtered signal (- - -).

and dotted lines, respectively. There are no differences observed between the first shell in both Fourier transforms, which proves that Fourier filtering errors can be completely avoided by using a slightly shorter range in k space than applied in the original forward Fourier transformation used in the filtering procedure.

3.4. Phase shifts and backscattering amplitudes derived from EXAFS data obtained from reference compounds

From equations (8)–(10) it can be seen that many parameters determine the final $\chi(k)$ function. In addition to the coordination number, distance and disorder, the backscattering amplitudes and phase shifts have to be known. On first sight, this seems to make data analysis rather complicated as so many parameters are unknown. However, it was found that the backscattering amplitude and phase shifts are transferable from one compound to the other, if the same absorber–backscatterer pair is involved [13]. Thus if a supported platinum catalysts is studied, a Pt foil can be used as a reference compound for Pt–Pt scattering amplitude and phase shifts. A compound can only be used as a reference if it has a uniform structure which is exactly known, for example from X-ray diffraction. The X-ray absorption spectrum is taken for this compound, and $\chi(k)$ is isolated according to the above described procedure. Then the Fourier transform of the data is taken and one coordination shell is specified to be isolated (see figure 7(a)). This will lead to

$$\chi_{\text{ref}}(k) = A_{\text{ref}}(k) \sin [\Phi_{\text{ref}}(k)] \quad (15)$$

with $A_{\text{ref}}(k)$ and $\Phi_{\text{ref}}(k)$ as known functions of k . As shown earlier and discussed before (12), the reliability range in k -space of $A_{\text{ref}}(k)$ and $\Phi_{\text{ref}}(k)$ is mainly determined by the k interval (from k_{min} to k_{max}) of the forward Fourier transform used in the Fourier filtering procedure. The reliability range of $A_{\text{ref}}(k)$ and $\Phi_{\text{ref}}(k)$ can generally be taken from $k_{\text{min,rel}} = k_{\text{min}} + 1$ to $k_{\text{max,rel}} = k_{\text{max}} - 1$.

Since the coordination number and distance are precisely known (for example $N_{\text{Pt–Pt}} = 12$ at 2.77 Å in a Pt foil) these can be used to extract a semi-backscattering amplitude ($F'(k)$) and total phase shift for the reference compound. The obtained $F'(k)$ is not the real backscattering amplitude $F(k)$, as it also contains the S_0^2 , Debye–Waller factor (σ) and electron mean free path (λ). S_0^2 and λ are also considered to be transferable from a reference compound. One can define

$$F'(k) = S_0^2 e^{-2R/\lambda} e^{-2k^2\sigma^2} F(k),$$

leading to

$$F'_{\text{ref}}(k) = \frac{A_{\text{ref}}(k)kR_{\text{ref}}^2}{N_{\text{ref}}}. \quad (16)$$

Equation (15) leads also to

$$\varphi_{\text{ref}}(k) = 2kR_{\text{ref}} - \Phi_{\text{ref}}(k). \quad (17)$$

The phase shift $\varphi_{\text{ref}}(k)$ and the backscattering amplitude $F'_{\text{ref}}(k)$ can now be determined using the experimentally determined functions $A_{\text{ref}}(k)$ and $\Phi_{\text{ref}}(k)$ and the known values of N_{ref} and R_{ref} . They can be used to analyse the EXAFS function of a sample with unknown structure. In practice, the reliability range for $\varphi_{\text{ref}}(k)$ and $F'_{\text{ref}}(k)$ obtained from reference EXAFS data of good signal to noise ratio is from $k_{\text{min}} = 3.5/4$ to $k_{\text{max}} = 12/15 \text{ \AA}^{-1}$.

3.5. Data analysis, obtaining R , N and $\Delta\sigma^2$, k -space and R -space fitting

Consistent with equations (16) and (17), the function that has to be minimised in the data analysis is

$$\chi_{\text{exp}}(k) - \sum_{j=1}^{\text{shells}} \frac{N_j}{k'_j R_j^2} e^{-2k'_j \Delta\sigma_j^2} F'_{\text{ref}}(k'_j) \times \sin [2k'_j R_j + \varphi_{\text{ref},j}(k'_j)], \quad (18)$$

where $\Delta\sigma^2$ is the Debye–Waller factor relative to that of the reference compound. Further, k' is a corrected wave vector to account for the difference in inner potential between the sample and the reference compound (ΔE_0):

$$k' = \sqrt{k^2 + \frac{2m_e}{\hbar} \Delta E_0}. \quad (19)$$

Several papers [14–16] have been published discussing the number of parameters that can be extracted from an EXAFS spectrum. The available data-range determines the number of free parameters that may be optimised according to the Nyquist theorem [16]:

$$\text{number of free parameters} = \frac{2\Delta k \Delta R}{\pi} + 2. \quad (20)$$

When fitting the full EXAFS spectrum (full Δk and ΔR range), the maximum number of independent parameters indicated from equation (20) can be less than the number of parameters needed to fit the total structure. This is because one has to include all shells in the data analysis, as well as all multiple scattering paths. One can avoid this problem by analysing only one or two particular co-ordination shells (i.e., choosing a small range of ΔR where it is known that just one or two shells contribute). Of course, equation (20) indicates that the number of free parameters must be reduced when limiting ΔR , however, the number of parameters required to fit just one or two shells is now also very much smaller.

The least squares fitting can be done in either k -space or in R -space [17]. When fitting in k -space one minimizes the variance:

$$k^n \text{ variance} = \frac{\int [k^n (\chi_{\text{model}}(k) - \chi_{\text{exp}}(k))]^2 dk}{\int [k^n \chi_{\text{exp}}(k)]^2 dk} \times 100, \quad (21)$$

where the $\chi_{\text{exp}}(k)$ in equation (20) is in most cases the χ obtained from the reverse transform of the chosen ΔR region of the full $\text{FT}_{\text{exp}}(R)$. This process is known as Fourier filtering to eliminate the extra shells from the $\chi(k)$ as discussed above. In R -space the variance between model and experiment are calculated for the imaginary and absolute parts by the expression

$$k^n \text{ variance} = \frac{\int [k^n (\text{FT}_{\text{model}}(R) - \text{FT}_{\text{exp}}(R))]^2 dR}{\int [k^n \text{FT}_{\text{exp}}(R)]^2 dR} \times 100, \quad (22)$$

where the integral over R is over just the limited chosen ΔR region. The variance or fit index should be below 1% to have a good fit of the experimental data in either case.

The difference between fitting in k -space and R -space is rather subtle, but very important, and the advantages lie with the R -space fitting. In k -space one has to reverse Fourier transform the experimental $\chi(k)$ over the chosen ΔR region in the Fourier filtering process. This introduces truncation errors at the outer regions of the data as discussed above, thereby reducing the reliable Δk -range. Taking the Fourier transform in either direction (forward or reverse) introduces truncation errors, but this truncation effect is not a problem in R -space fitting, because the chosen ΔR region is much smaller than the total R range anyway. Secondly, the noise build up problem is minimized in R -space fitting, since the model function has no noise in it. However, in k -space fitting, one has to forward, then reverse the Fourier transform process on the experimental data. Although this eliminates the high-frequency noise and higher shells, it can increase the relative magnitude of the low-frequency noise. Thirdly, and perhaps most important, in k -space fitting the variance defined in equation (20) has many maxima and minima. This is because the $\chi(k)$ function is an oscillatory function so that if the wavelength of the model and experimental χ are not very similar, the two functions go in and out of phase, introducing many hills and valley in the variance function. Of course the FT(R) in the chosen ΔR range has normally just one maximum in it. Thus the least-squares iterative process is much more stable and the problem of converging to a relative minimum rather than the true minimum is much less probable in R -space fitting.

There are several ways to judge the quality of the fit after achieving convergence. One should always compare the model fit and the experimental data both in R - and k -space. In R -space, both the imaginary part and the amplitude of the Fourier transform is used in fitting the spectra. The amplitude depends on the co-ordination number and disorder, whereas the imaginary part is mainly determined by the interatomic distance and the inner potential correction. Thus the imaginary part is very sensitive for judging the quality of the fit, since a misfit shows up immediately in the appearance of wrong nodes in the imaginary part of the Fourier transform. Moreover, comparison in R -space easily reveals the effect of overlapping shells. Comparison in k -space even more dramatically reveals errors in the fit if the wavelength or amplitude of the model $\chi(k)$ is not the same as the experimental one.

The fit quality can also be examined mathematically as defined by the Goodness of Fit [21] function:

$$\text{Goodness of Fit} = \varepsilon_{\nu}^2 = \frac{P}{\text{NPTS}(P-p)} \sum_i^{\text{NPTS}} \left(\frac{\chi_{\text{exp}}^i - \chi_{\text{model}}^i}{\sigma_{\text{exp}}^i} \right)^2. \quad (23)$$

Here P is the total number of free parameters [21], p the number of free parameters that have been refined, and NPTS is the actual number of points in the k -range used for analysis, σ_{exp} is the standard deviation for each data point, obtained by averaging several scans of one experiment, which improves the signal to noise ratio of the final $\chi(k)$.

Often the standard deviation in the experimental data is very small, as it only represents statistical errors. As a result, the ε_{ν}^2 values are extremely high. In that case systematic errors (e.g., experimental uncertainty) should be added to those standard deviations obtained by averaging scans [22]. When the structural error is not known, variances in both k - and R -space less than 1% are indicative of model spectra that fit the experimental data closely.

To check whether one model describes the data better than a second model, a so-called F -test can be applied [23,24]. In this way, a probability percentage can be obtained for the likelihood of a model. However, when data analysis is performed in R -space, without using the complete R -range, no useful information can be obtained from the F -test, as it is calculated in k -space over the whole available range.

The XDAP-program also provides a possibility to calculate statistical errors in and correlation between parameters [23]. The calculations are based on the experimental standard deviation, which in many cases is too low to account for systematic errors. This results in estimated or calculated (mathematical) errors in the parameters that are too small (often less than 0.1%). Recently, a study was published on the reliability of parameters obtained by XAFS data-analysis [25]. Based on their results, the errors in many instances are estimated to be 5% in coordination number (N), 1% in distance (R), 5% in Debye–Waller factor ($\Delta\sigma^2$) and 10% in inner potential correction (E_0).

3.6. The use of theoretical references

The scattering amplitude of the low Z atoms decays rapidly with increasing values of k as shown in figure 4. For an accurate analysis of the low Z contributions in the EXAFS data, phase shifts and backscattering amplitudes have to be reliable down to low values of k . Moreover, recent papers [10,11,26–28] have shown and in this issue [2] it is further demonstrated that very important electronic information can be obtained from atomic XAFS data. Atomic XAFS features have low frequency oscillations and a rapid decaying amplitude with increasing values of k . Thus, the AXAFS oscillations have amplitudes comparable to normal EXAFS only at very low values of k ($k \leq 4 \text{ \AA}^{-1}$). In order to separate the AXAFS oscillations from the regular EXAFS, the calculated first-shell EXAFS contributions are subtracted from the experimental data. It is of crucial importance that the first-shell EXAFS contributions be determined accurately down to very low values of k to ensure that the AXAFS resulting from the subtraction procedure is also reliable at very low values of k .

As already mentioned above, the phase shifts and backscattering amplitudes derived from EXAFS data obtained from reference compounds are not reliable for values of k lower than 3.5 \AA^{-1} . Spherical-wave multiple-scattering codes are available to calculate the phase shifts and backscattering amplitudes, which are reliable down to $k = 2\text{--}2.5 \text{ \AA}^{-1}$. It is now possible to calibrate the *ab ini*-

tio results with the experimental EXAFS data obtained from reference compounds and using R -space fitting as discussed above.

This general procedure is demonstrated here for determining the Pt–Pt and Pt–O phase shifts and backscattering amplitudes from Pt foil [29] and $\text{Na}_2\text{Pt}(\text{OH})_6$ [30], respectively. Theoretical phase and backscattering amplitudes for the Pt–Pt and Pt–O absorber–scattering pairs were generated utilising the FEFF7 code [31]. Figure 8 (a) and (b) show the Fourier transforms (k -weighted, $k = 2.5\text{--}15 \text{ \AA}^{-1}$ and $k = 2.5\text{--}13 \text{ \AA}^{-1}$ for Pt foil and $\text{Na}_2\text{Pt}(\text{OH})_6$, respectively) of the measured EXAFS spectra for the Pt foil and $\text{Na}_2\text{Pt}(\text{OH})_6$ after normalisation and background removal.

The XDAP [23] program was used for the data fitting. In this code the Debye–Waller factor is given as an offset with respect to the reference (see equation (18)). The first-shell contributions have been fitted using the theoretical references. The theoretical references as generated were optimised so that the offset in the Debye–Waller factor is approximately zero. The value of S_0^2 was determined by assuring that the first-shell fit results in the cor-

rect co-ordination number for both samples with the offset in the Debye–Waller factor set to zero. Also, the potential used and the parameters V_r and V_i are chosen so that the backscattering amplitudes and phase shifts reproduce as much as possible the experimental references [23]. The imaginary part of the potential, V_i , takes into account the experimental broadening, and the real part, V_r , the offset in the zero position of the energy with respect to the absorption edge. Changing V_r mainly affects the intensity of the calculated white line, and the value of ΔE_0 found in the fit procedure.

The best agreement between experimental and calculated results for Pt–Pt and Pt–O scattering was found when the Dirac–Hara exchange correlation potential was used, in contrast to Zabinsky et al. [31], who concluded over all that the Hedin–Lundquist model was better. However, we have concentrated exclusively on the first-shell data in the reference calculations. Similarly, Ankudinov [32] found for a simulation of Cu foil, that when calculating the single scattering phase shift and allowing for a correction to E_0 , better agreement between experiment and calculation could be obtained with the Dirac–Hara self-energy model rather than with the Hedin–Lundquist model. In FEFF7, the parameter V_r is used for this E_0 correction. For both the Pt–Pt and Pt–O references, an additional 3 eV had to be added to the core-hole lifetime to account for instrumental broadening. This is in good agreement with the estimated 3.5 eV energy resolution of the experimental setup. The final input parameters for FEFF7 are given in table 1.

The fits in R -space (k -weighted, $\Delta k = 2.5\text{--}15 \text{ \AA}^{-1}$ and $\Delta R = 1.5\text{--}3.2 \text{ \AA}$ for Pt foil; $\Delta k = 2.5\text{--}13 \text{ \AA}^{-1}$ and $\Delta R = 1.3\text{--}1.9 \text{ \AA}$ for $\text{Na}_2\text{Pt}(\text{OH})_6$) using the optimised theoretical phase shifts and backscattering amplitudes are shown in figure 8 (a) and (b) (dotted lines) for Pt foil and $\text{Na}_2\text{Pt}(\text{OH})_6$, respectively. The results of the fit are given in table 2. It can be seen that the fitted EXAFS co-ordination parameters correspond with the crystallographic

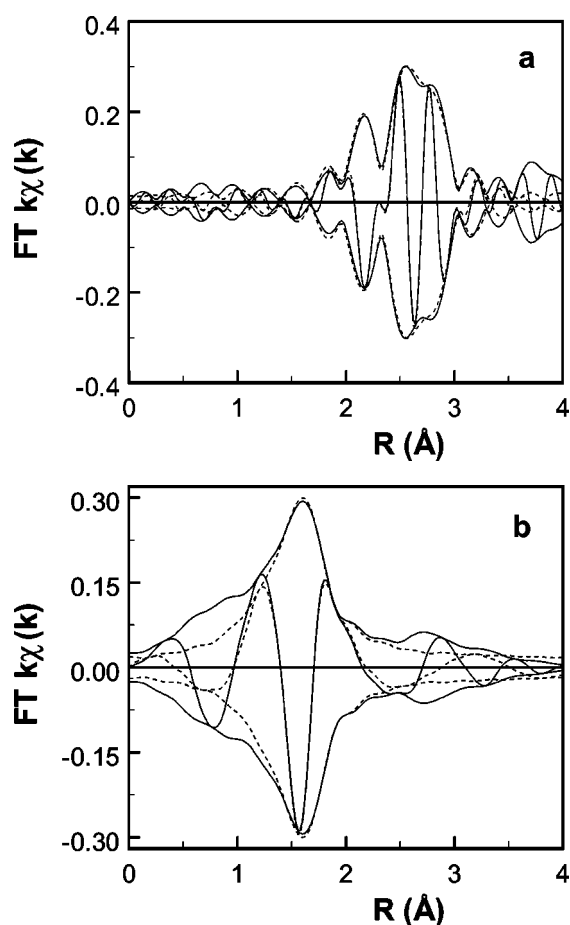


Figure 8. (a) Fourier transform (k^1 , $\Delta k = 2.5\text{--}15 \text{ \AA}^{-1}$) of the experimental EXAFS (—) and first-shell fit (---) for Pt foil; (b) Fourier transform (k^1 , $\Delta k = 2.5\text{--}13 \text{ \AA}^{-1}$) of the experimental EXAFS (—) and first-shell fit (---) for $\text{Na}_2\text{Pt}(\text{OH})_6$. In both cases multiple electron excitations were removed from the EXAFS spectrum. Theoretical references were used for phase shifts and backscattering amplitudes.

Table 1

Parameters used in the calculations for the generation of the theoretical references.

Atom pair	Potential	σ^2 (\AA^2)	S_0^2	V_r (eV)	V_i (eV)
Pt–Pt	Dirac–Hara	0.00234	0.82	–4.2	3.0
Pt–O	Dirac–Hara	0.00342	0.90	0.0	3.0

Table 2

Best fit result for the experimental data using the theoretical references. Two different background procedures were used, in which the double electron excitation (DE) was either kept in the oscillatory part of the spectrum or extracted with the background. Fit was performed in R -space, k -weighted; $\Delta k = 2.5\text{--}15 \text{ \AA}^{-1}$, $\Delta R = 1.5\text{--}3.2 \text{ \AA}$ for Pt foil and $\Delta k = 2.5\text{--}13 \text{ \AA}^{-1}$, $\Delta R = 1.3\text{--}1.9 \text{ \AA}$ for $\text{Na}_2\text{Pt}(\text{OH})_6$, respectively.

Atom pair	N	R (\AA)	$\Delta\sigma^2$ (\AA^2)	E_0 (eV)
Pt–Pt	11.68	2.766	–0.00004	0.08
Pt–O	6.14	1.997	–0.00004	4.80

values. However, the obtained Pt–O distance of 2.00 is 0.05 shorter than the crystallographic average, which is beyond the above mentioned limits of accuracy of 0.02 Å. Obviously, the theoretical Pt–O phase shifts are somewhat less accurate in this case. However, the generated theoretical Pt–Pt and Pt–O references are now calibrated and can be used to a significantly lower k -value than the previously used experimental references. We were able to fit the χ_{EX} down to a lower limit of about 2.5 \AA^{-1} . The previously extracted and used experimental references were only good for $k > 3.5 \text{ \AA}^{-1}$ due to Fourier filtering errors. The gain at low k , as already discussed above, is especially important for the analysis of the EXAFS phenomenon. The result is a better isolation of the EXAFS peak at low R (see further [2]).

3.7. Detection of low Z scatterers, use of k^1 and k^3 weighting

One has to realise that both high Z (e.g., metal–metal) and low Z (e.g., metal–oxygen) contributions are present in the EXAFS data collected on metal particles dispersed on high surface area supports. The low Z contributions may arise from the support or from adsorbates present on the surface of the metal particles. It is tempting to apply a k^2 or k^3 weighting to the EXAFS spectrum to compensate for the decay in amplitude of the spectrum with k . A function, which has an equalised amplitude over the entire k -range results gives narrower peaks in the Fourier transform, which are easier to separate. This weighting by k^2 or k^3 emphasises the high Z contributions to the spectrum since high Z elements have more scattering power at high values of k than low Z elements. Therefore, the use of a k^2 or k^3 weighted EXAFS spectrum or Fourier transform makes the analysis much less sensitive to the presence of low Z contributions in the EXAFS data.

An example is given in figure 9. Figure 9(a) (solid line) shows the k^3 -weighted Fourier transform of $\chi_{\text{exp}}(k)$ for a Pt/ γ -Al₂O₃ catalyst reduced at 573 K, evacuated at the same temperature and measured at 100 K [33]. The best-fit Pt–Pt contribution, indicated with the dotted line, corresponds especially well to the imaginary part of the k^3 -weighted Fourier transform of the experimental data in the range $2 < R < 3 \text{ \AA}$. The best-fit Pt–Pt contribution and experimental k^1 -weighted Fourier transforms (figure 9(b)) show much larger differences (both in magnitude and imaginary part). These differences are due to the presence of low Z contributions (O) from the support and atomic XAFS [2]. From figure 9 it is obvious that for a proper analysis of the low Z contributions, which might be present in the EXAFS spectra, k^1 -weighted fits and/or Fourier transforms should be utilised.

3.8. Phase- and amplitude-corrected Fourier transforms

The phase factor $\Phi(k)$ and the backscattering amplitude $F(k)$ are both functions of k . This implies that the Fourier

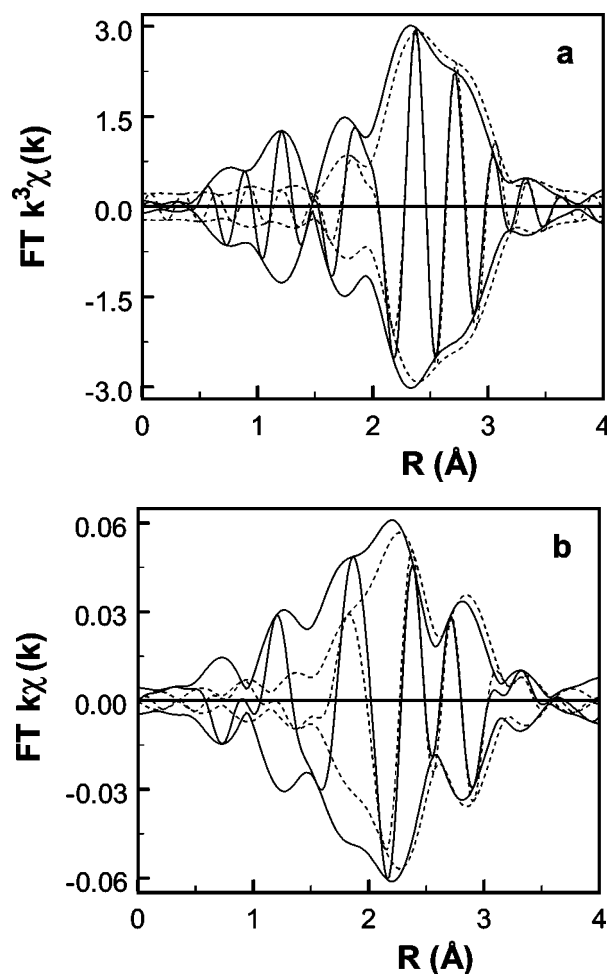


Figure 9. (a) k^3 and (b) k^1 Fourier transform ($\Delta k = 2.5\text{--}11 \text{ \AA}^{-1}$) of the experimental EXAFS (—) of a Pt/ γ -Al₂O₃ catalysts [33] (reduced at 573 K, evacuated at the same temperature and measured at 100 K) and first-shell Pt–Pt fit (---).

transformation of the EXAFS function does not lead to an optical transform (i.e., a transform with constant phase and amplitude). Generally, the peaks of the Fourier transform of an EXAFS function are asymmetric. For high Z elements, the k -dependence of the phase and the backscattering amplitude may even lead to the appearance of multiple or satellite peaks in the Fourier transform of an EXAFS function describing a single absorber–backscatterer pair. This can clearly be seen in the k^1 -weighted Fourier transform of the Pt–Pt first-shell data extracted from Pt foil and the Pt/ γ -Al₂O₃ catalysts in figures 8(a) and 9(b). First-shell Pt–Pt peaks appear at three different values of R . This has led in the past to much confusion in analysing EXAFS data containing contributions of high Z elements, since these shoulders were interpreted as physically important peaks arising from other scatterers. However, for the Pt/ γ -Al₂O₃ catalysts, contributions from other scatterers in the support cannot be completely excluded. It can be seen in figure 9(b) that indeed the Fourier transform of $\chi(k)$ for the Pt catalysts is more asymmetric at lower values of R than that of the pure Pt–Pt scattering due to the presence of the low Z

scatterers. To investigate this further, optical Fourier transforms can be used.

A normal Fourier transform can be converted to an optical transform by removing the phase function and the backscattering amplitude. A phase- and amplitude-corrected (optical) Fourier transform can be obtained by transformation of the following function [34,35]:

$$\chi(k) \frac{e^{-i\varphi(k)}}{F(k)}. \quad (24)$$

Application of a phase- and amplitude-corrected Fourier transform leads to a single peak with a symmetrical imaginary part, having its maximum at the top of the absolute magnitude and at the right coordination distance. The use of optical Fourier transforms can be of great help [36] in the identification of different types of neighbours by application of different phase and/or amplitude corrections. A phase- and amplitude-corrected Fourier transform for an X–Y absorber–backscatterer pair must have a positive imaginary part peaking around the maximum of its magnitude if the EXAFS function indeed originates from an X–Y pair. This can be seen in figure 10(a), which displays the Pt–Pt phase- and amplitude-corrected Fourier transform (k^1 , $\Delta k = 3\text{--}11 \text{ \AA}^{-1}$) of the first-shell region of Pt foil. Both the magnitude as well as the imaginary part are symmetric. A phase- and amplitude-corrected Fourier transform, which is still not symmetrical, can be a strong indication that more than one contribution is present. This is demonstrated in figure 10(b), which shows the Pt–Pt phase- and amplitude-corrected Fourier transform of the Pt/ γ -Al₂O₃ catalysts (solid line). Both the magnitude and the imaginary part are now not symmetric. The Fourier transform of the fitted Pt–Pt contribution is also given (dotted line). A small inner potential correction of 1.4 eV, which was necessary to fit the Pt–Pt contribution, makes the imaginary part slightly asymmetric.

3.9. Difference file technique

Another useful tool is the difference file technique [12,34]. In general, the experimental $\chi_{\text{EXP}}(k)$ data can be described by summation of different model EXAFS functions $\chi_{\text{MOD},j}(k)$, describing each co-ordination shell:

$$\chi_{\text{EXP}}(k) = \sum_{j=1}^{\text{Shells}} \chi_{\text{MOD},j}(k). \quad (25)$$

When fitting shell m , one can derive the following expression between the sum of the remaining model EXAFS functions and the experimental EXAFS:

$$\chi_m = \chi_{\text{EXP}} - \sum_{i=1; i \neq m}^j \chi_{\text{MOD},i}, \quad (26)$$

where the right side of equation (25) defines the difference spectrum. By comparing the contribution χ_m with the difference spectrum, the fit quality can be determined

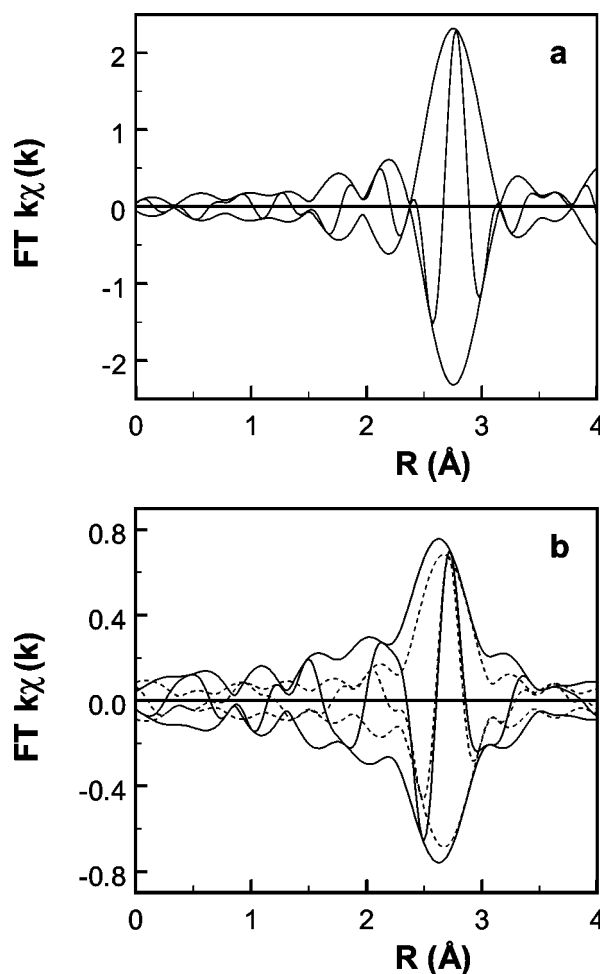


Figure 10. (a) Fourier transform (k^1 , $\Delta k = 3.0\text{--}11 \text{ \AA}^{-1}$, Pt–Pt phase and amplitude corrected) of EXAFS data of Pt foil; (b) Fourier transform of (k^1 , $\Delta k = 3.0\text{--}11 \text{ \AA}^{-1}$, Pt–Pt phase and amplitude corrected) of EXAFS data the Pt/ γ -Al₂O₃ catalysts [33] (—) and first-shell Pt–Pt fit (- - -).

for this one contribution. This is an important analysis procedure when analysing an experimental EXAFS spectrum for which the different contributions have very different magnitudes. Examples include the EXAFS data obtained from catalysts, which consist of metal particles, metal sulfides and metal oxides dispersed onto different supports. Often, the first peak in the Fourier transform of the EXAFS data measured on supported metal particles will be due to a metal–metal contribution highly overlapped with a metal–support oxygen contribution. The peaks overlap even though the metal–metal and metal–oxygen distances are different due to the different energy dependence of the phase shifts for the absorber–backscatterer pairs. For medium sized metal particles, the metal–metal contribution will be much larger in intensity than the metal–support oxygen contribution. By using different k weightings and phase and amplitude corrections, it is now possible to separate both contributions from each other and from higher order contributions. An example of the difference file technique is shown in figure 11. In figure 11(a) the total fit (Pt–Pt + Pt–O) in R -space (k^1 , $\Delta k = 3\text{--}11 \text{ \AA}^{-1}$) is plotted

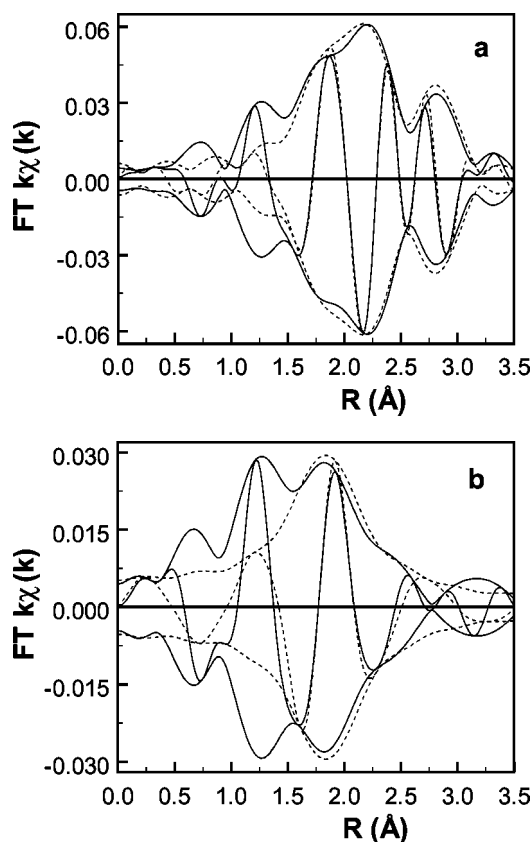


Figure 11. (a) Fourier transform (k^1 , $\Delta k = 3.0\text{--}11 \text{ \AA}^{-1}$) of EXAFS data of the Pt/ γ -Al₂O₃ catalysts [33] (—) and total fit (Pt–Pt + Pt–O) (---). (b) Fourier transform (k^1 , $\Delta k = 3.0\text{--}11 \text{ \AA}^{-1}$, Pt–O phase corrected) of difference spectrum (raw EXAFS minus fitted Pt–Pt contribution) and fitted Pt–O contribution.

with a dotted line. The Fourier transform of the difference file ($\chi_{\text{EXP}} - \chi_{\text{Pt-Pt}}$) is displayed in figure 11(b) with a solid line. The Fourier transform of the best-fit Pt–O contribution describes the difference file for $1.5 < R < 2.5 \text{ \AA}$. The differences at lower values of R are due to the EXAFS part of the spectrum [2]. The difference file technique is a very powerful method. Small errors in the model EXAFS functions of the larger contribution to the total EXAFS will immediately show up in the difference file.

The assignment of the weak EXAFS contributions as arising from the metal–support interface and the inner potential values for the metal–oxygen support contribution, as used in some of our articles, was questioned recently [37]. In [38] we show by using the difference file technique, that the presumptions stated in [37] by these authors in fact are not valid, so that we believe the analysis we originally reported is still correct.

3.10. Correlation between N and $\Delta\sigma^2$. Use of both k^1 - and k^3 -weighted Fourier transforms

The determination of a unique set of co-ordination parameters for a particular contribution to an EXAFS spectrum is often difficult due to the high correlation between the value of the co-ordination number N and the Debye–

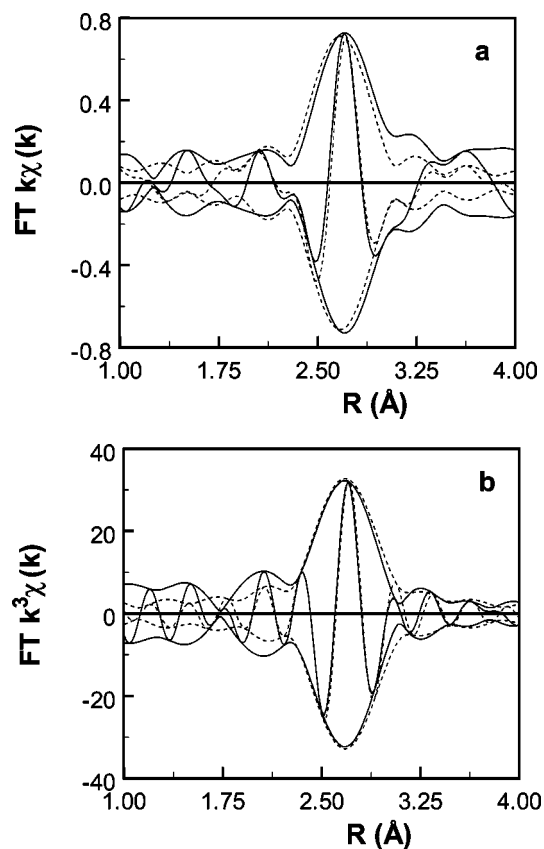


Figure 12. (a) k^1 and (b) k^3 Fourier transform ($\Delta k = 3.0\text{--}11 \text{ \AA}^{-1}$, Pt–Pt phase and amplitude corrected) of difference spectrum (raw EXAFS minus fitted Pt–O contribution) and fitted Pt–Pt contribution.

Waller factor $\Delta\sigma^2$ (i.e., different combinations of N and $\Delta\sigma^2$ can lead to similar quality fits). However, this set of combinations depends on the k weight factor, which has been used for the Fourier transform [12]. In [12,36], it has been shown that by simultaneous minimisation of the variance, equation (18), in a k^1 - and k^3 -weighted Fourier transform, a unique set of parameters can be found, and further, that a good fit is required with both weightings before one can trust the final results. It is essential to use phase- and amplitude-corrected Fourier transforms when applying this method, because otherwise the asymmetry of the peaks will obscure the results. An example of this approach is given in figure 12. Figure 12(a) (solid line) gives the Pt–Pt phase- and amplitude-corrected Fourier transform (k^1 , $\Delta k = 3\text{--}11 \text{ \AA}^{-1}$) of the difference file ($\chi_{\text{EXP}} - \chi_{\text{Pt-O}}$) of the Pt/ γ -Al₂O₃ catalysts discussed above, together with the fitted Pt–Pt contribution (dotted line). In figure 12(b) the comparable data for the k^3 -weighted case is shown. It can be seen that good agreement exists with both weightings. This demonstrates that the Pt–Pt contribution is fit with a unique combination of N and $\Delta\sigma^2$.

4. Conclusions

In this paper an intuitive picture of the physical principles of electron scattering that produce the contributions

to the phase and the scattering amplitude is given. Some of the more innovative tools of EXAFS data analysis are presented such as: (a) fitting in R -space, (b) application of the difference file technique, (c) control of the fit procedure with k^1 and k^3 weighting with the help of phase- and amplitude-corrected Fourier transforms, (d) the use of theoretical references, and (e) the detection of low Z scatterers. Illustrations have been given to show that these basic analysis tools can provide information on not only the structure of the supported metal particles, but also the interaction between the metal particles and the support.

Acknowledgement

The authors would like to thank the scientific staff of beamline BM29 of the ESRF (Grenoble, France) and beamline 9.2 of the SRS (Daresbury, UK) for their continuing interest and stimulating support.

References

- [1] J.E. Müller and J.W. Wilkins, Phys. Rev. B 29 (1984) 4331.
- [2] D.E. Ramaker, G.E. van Dorssen, B.L. Mojet and D.C. Koningsberger, Topics Catal. 10 (2000) 157.
- [3] P.A. Lee and J.B. Pendry, Phys. Rev. B 11 (1975) 2795.
- [4] S.J. Gurman and R.F. Pettifer, Phil. Mag. B 40 (1979) 345.
- [5] D.E. Sayers, E.A. Stern and F.W. Lytle, Phys. Rev. Lett. 27 (1971) 1204.
- [6] B.K. Teo, *EXAFS: Basic Principles and Data-analysis* (Springer, New York, 1986).
- [7] D.C. Koningsberger and R. Prins, eds., *X-ray Absorption* (Wiley, New York, 1988).
- [8] F. Szmulowicz and D.M. Pease, Phys. Rev. B 17 (1978) 3341.
- [9] J.W. Cook, Jr. and D.E. Sayers, J. Appl. Phys. 52 (1981) 5024.
- [10] D.E. Ramaker, B.L. Mojet, W.E. O'Grady and D.C. Koningsberger, J. Phys. Condens. Matter. 10 (1998) 1.
- [11] B.L. Mojet, J.T. Miller, D.E. Ramaker and D.C. Koningsberger, J. Catal. 186 (1999) 373.
- [12] D.C. Koningsberger, in: *Neutron and Synchrotron Radiation for Condensed Matter Studies*, Vol. II, eds. J. Baruchel, J.L. Hodeau, M.S. Lehmann, J.R. Regnard and C. Schlenker (Springer, Berlin, 1994) p. 213.
- [13] B.A. Bunker and E.A. Stern, Phys. Rev. B 27 (1983) 1017.
- [14] P.A. Lee, P.H. Citrin, P. Eisenberger and B.M. Kincaid, Rev. Mod. Phys. 53 (1981) 769.
- [15] R.W. Joyner, K.J. Martin and P. Meehan, J. Phys. C 20 (1987) 4005.
- [16] E.A. Stern, Phys. Rev. B 48 (1993) 9825.
- [17] T.M. Hayes and J.B. Boyce, Solid State Phys. 237 (1982) 283.
- [18] P.A. Lee, P.H. Citrin, P. Eisenberger and B.M. Kincaid, Rev. Mod. Phys. 53 (1981) 769.
- [19] R.W. Joyner, K.J. Martin and P. Meehan, J. Phys. C 20 (1987) 4005.
- [20] E.A. Stern, Phys. Rev. B 48 (1993) 9825.
- [21] F.W. Lytle, D.E. Sayers and E.A. Stern, Physica B 158 (1988) 701.
- [22] E. Stern, M. Newville, B. Ravel, Y. Yacobi and D. Haskel, Physica B 208/209 (1995) 117.
- [23] M. Vaarkamp, J.C. Linders and D.C. Koningsberger, Physica B 208/209 (1995) 159.
- [24] N.R. Draper and H. Smith, *Applied Regression Analysis* (Wiley, New York, 1966).
- [25] G.G. Li, F. Bridges and C.H. Booth, Phys. Rev. B 52 (1995) 6332.
- [26] D.C. Koningsberger, J. de Graaf, B.L. Mojet, J.T. Miller and D.E. Ramaker, Appl. Catal. 191 (2000) 205.
- [27] W.E. O'Grady and D.E. Ramaker, Electrochim. Acta 44 (1998) 1283.
- [28] D.E. Ramaker, X. Qian and W.E. O'Grady, Chem. Phys. Lett. 299 (1999) 221.
- [29] R.W.G. Wyckoff, *Crystal Structures*, Vol. 1, 2nd Ed. (Wiley, New York, 1963) p. 10.
- [30] M. Trömel and E. Lupprieh, Z. Anorg. Chem. 160 (1975) 414.
- [31] S.I. Zabinsky, J.J. Rehr, A. Ankudinov, R.C. Albers and M.J. Eller, Phys. Rev. B 52 (1995) 2995.
- [32] A. L. Ankudinov, Ph.D. thesis, University of Washington (1996).
- [33] G.E. van Dorssen, Ph.D. thesis, Utrecht University (1999).
- [34] J.B.A.D. van Zon, D.C. Koningsberger, H.F.J. van't Blik and D.E. Sayers, J. Chem. Phys. 82 (1985) 5742.
- [35] F.W. Lytle, R.B. Greegor, E.C. Marques, D.R. Sandstrom, G.H. Via and J.H. Sinfelt, J. Catal. 95 (1985) 546.
- [36] F.W.H. Kampers, Ph.D. thesis, University of Technology (1988).
- [37] A. Michalowicz and G. Vlaic, J. Synch. Rad. 5 (1998) 1317.
- [38] J.H. Bitter and D.C. Koningsberger, J. Synch. Rad., submitted.